

# Development of Amorphous Ribbon Manufacturing Technology

CHUNG-YUNG WU\*, KUAN-JU LIN\*, YI-TING CHENG\*, CHUN-KUEI HUANG\*,  
CHIEN-NAN PAN\*\*, WEN-CHIEH LI\*, LIEN-KUEI CHIANG\*, CHE-NAN YEH \*\*  
and SHIH-CHIEH FONG \*

\* Iron and Steel Research & Development Department  
\*\* New Materials Research & Development Department  
China Steel Corporation

## ABSTRACT

Iron-based amorphous ribbons exhibit excellent soft magnetic properties and are used in high efficiency transformers, which are the key components for energy saving in a power grid. Manufacturing technology of the ribbon has since been limited in the market and that necessitates the fundamental development of associated engineering. This article reports on an implementation of a pilot scale ribbon casting line at China Steel (CSC), which consists of a melter, holder, crucible, casting wheel and winder. Their functions are described and among which melt flow metering, atmosphere control, cooling rate estimation, tension control and the refractory are further discussed. Experimental work demonstrated the current system is capable of controlling the casting pressure within 1.5%, oxygen concentration rate below 1%, cooling the ribbon at the rate of  $1.77 \times 10^6$  °C/s, and winding the ribbon at a speed of 1200 m/min. The ribbon quality was evaluated by an optical microscope and comparatively studied using two controlling factors including the wheel surface roughness and casting pressure. The ribbon magnetic properties were measured by a VSM. Improvement in hysteresis loss and embrittlement during the annealing process are addressed. Appropriate annealing temperature range is recommended.

**Keywords:** Planar flow casting, Amorphous

## 1. INTRODUCTION

Iron-based amorphous ribbons were known for their superior magnetic properties in terms of extremely low iron losses comparing to other commercially available soft magnetic materials. Therefore, they are ideal materials for the iron cores of high-grade distribution transformers, which play an important role in improving power grid efficiency and reducing greenhouse gas emission<sup>(1)</sup>. In the last 10 years as climate change and global warming has become our greatest challenge to resolve, the rapidly increasing need for an efficient core material has drawn increasing attention to the industry. However, the resources for such a technological development were scarce. During the 1980s and 1990s, numerous researches were devoted to amorphous material development, manufacturing technologies, and ribbon applications. Amorphous research groups, however, had shrunk significantly during the late 90's due to low petroleum prices which discouraged the usage of energy-saving facilities and the low-loss amorphous ribbons.

That eventually led to declining interest by the research population. Meanwhile the scale of development of commercial ribbon manufacturing processes faced severe engineering challenges and only a very limited number of successful cases were reported. Circumstances were that the off-the-shelf manufacturing technology was not readily available and a ground up development was necessary. This research was dedicated to laying a technical foundation for commercial scale ribbon manufacturing. The project's focus aligned with China Steel's long term commitment in the field of green products and chose the iron-based amorphous ribbon as the target for development.

Forming amorphous texture requires extremely high cooling rates of a melt in the order of  $10^5$  to  $10^6$  °C/s. Methods that meet these requirements includes splat quench, twin-roll casting, single roll free jet and melt spinning casting<sup>(2)</sup>. The primary ribbon casting process rooted in the planar flow casting. The melt was extruded from a confined slit to a high-speed rotating cooling drum so that the liquid metal was extracted in a

thin layer of film to facilitate heat extraction. The concept has been implemented on a laboratory scale as seen in many applications<sup>(3)</sup>. The fundamental concept was realized in a much greater scale as a pilot plant at CSC. Immense engineering issues were involved in its development. Selected items are highlighted and presented in this report.

## 2. OVERVIEW OF THE IMPLEMENTED SYSTEM

A pilot plant consisting of a melter, holder, crucible, cooling wheel, and winder was established at CSC. Its schematic diagram is shown in Fig.1. The melter was an induction furnace capable of heating 200 kg of cold charge to tapping readiness in an hour. Element oxidation would occur as no atmosphere control was applied on the open top of the furnace. Oxides comprised melt slag was removed before the melt was poured into the holder. Metal loss and compensation was necessary based on pre-calibration results.

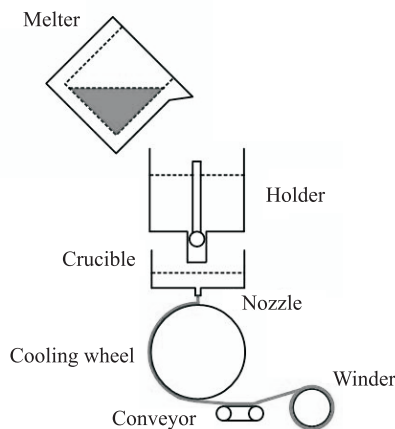


Fig.1. Schematic drawing of the amorphous ribbon casting line.

The holder is a holding furnace and acts as a melt reservoir with a shallow depth. Its primary function is to improve the cleanness of the melt because inclusions could have strong impacts on the casting process and ribbon quality. This was achieved by holding the melt for a substantial amount of time for allowing the particles, such as inclusions and impurities, to displace to the liquid surface by buoyant forces and preventing them from the downstream process. The appropriate holding time could be estimated by combining the liquid depth and the traveling speed of a particle using the Stoke equation (Eq.1),

$$V_t = \frac{gd^2(\rho_m - \rho_p)}{18\mu} \dots\dots\dots (1)$$

where  $V_t$  is the terminal speed,  $\mu$  viscosity of the liquid,  $g$  gravity,  $d$  diameter of the particle,  $\rho_m$  and  $\rho_p$  the liquid and particle density, respectively.

The crucible acts as a flow rate control buffer, which allows the accumulating melt up to 50 kg to be pressurized by external inert gas or static pressure so to be injected through the nozzle. The crucible also serves as a temperature controller where the melt temperature might be reheated to an appropriate superheat by an induction coil. Care was exercised to select a proper induction frequency so not to generate excessive flow field perturbation and affecting the puddle stability. One of the most important features in the crucible is the nozzle, which is the last component in the flow path and governs the melt curtain shape and constrains the puddle along with the wheel. The nozzle at the current pilot plant permits a maximum ribbon casting width of 150 mm.

The casting wheel is the primary heat extraction device being made of high strength copper C17200. It was equipped with an internal active cooling system so to withdraw the maximum melt heat during a long cast campaign. Several auxiliary accessories not shown in the schematic including a peeling device, surface texture control device and ribbon guiding air also play important roles in stabilizing the process. Before leaving the wheel, the liquid was assumed to be quenched to a less fluidic state to form a ribbon.

The ribbon departing from the wheel at a given angular position was taken by a moving belt with attraction forces. Its moving direction and speed was fully supported by the belt. It was subsequently delivered to the winder in a manner that the grabbing device is able to attach it to the winder.

The winding system is composed of three major subsystems, i.e. ribbon grabber, head remover, and tension controller. Due to the high traveling speed of the ribbon in the range of 20 to 30 m/s, these mechanisms are required to be agile and precise. Successful realization includes both mechanically and magnetically actuated grabbers, high speed swaying synchronous knife, and mixture of speed and torque control modes.

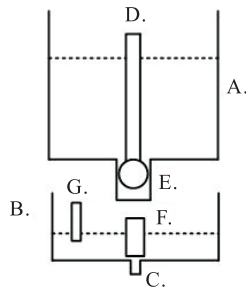
## 3. IMPLEMENTATION

### 3.1 Melt flow metering

During the amorphous ribbon casting process, one of the critical requirements was to maintain the flow rate stability of the molten metal through the casting nozzle. Molten metal flow rate in the casting process was governed by several factors, including the gap between the cooling wheel and nozzle; the wheel surface speed and the injecting pressure. For the system developed at CSC, the injecting pressure was primarily controlled by the liquid level in the crucible

which highlighted the importance of the level control.

Figure 2 shows the schematic diagram of the level control system. A control rod was used to regulate the flow rate from the holder to the crucible. A level detector in the crucible was used to monitor the true level for control feedback. A stopper was used simply as a valve to start/stop the process and served no function during casting. A block diagram of the level feedback control system was established as shown in Fig.3, where the crucible is the control plant, the input and output are the flow rates of the holder and nozzle, respectively, and the feedback is the level signal.



A. Holder, B. Crucible, C. Nozzle, D. Control rod, E. SEN, F. Stopper, G. Level detector

Fig.2. Structure of the level control system.

Owing to multiple devices along the flow path, there exists a system delay affecting control precision. This delay could be highly variant because the molten metal mobility is influenced by the channel temperature significantly. The level controller was designed using a rule table method to overcome process uncertainties. The control rod, the primary actuator, operated at an on-off fashion with variable discrete strokes and speeds, which were determined by level errors and preset prior to the experiment. Figure 4 shows the operating sequence that details the control rod movement.

A partition of Cast #1036 demonstrates the effectiveness and precision of the proposed level control method (Fig.5). At the initial stage, the target level was set at 180 mm and the control rod opened for an

extended period of time to fill the crucible chamber. The true level reached its target with a 4.4% error, which was acceptable as the start of a cast experienced a transient state of temperature and flow field. At the second stage, the molten metal level was raised to 200 mm and the level reached 203 mm with a steady state error of 1.5%. The control rod operated at a lower frequency and stroke as the errors were converging. Note that the true level of the crucible continued fluctuating in the range of 1 mm. The controller was not activated due to its fuzzy nature. This demonstrates the accuracy and robustness of the designed control system.

3.2 Atmosphere control

Atmosphere control by argon gas in the steelmaking process is a common practice to prevent molten steel being contaminated by oxygen or nitrogen. Both theoretical analysis and off-line tests were realized for this preliminary study. The empirical equation developed in this research was based on a well-mixed flow model<sup>(4)</sup> (Eq.2). The atmosphere control (or oxygen content) can be expressed as a function of the container volume (V) and the gas volumetric flow rate (Q),

$$[O_2](t) = [O_2]_{initial} \times e^{-\frac{Q}{V}t} + \alpha \times \frac{V}{Q^\beta} \times \left( 1 - e^{-\frac{Q}{V}t} \right)$$

..... (2)

An off-line test platform was developed to simulate the working environment. A well-sealed container with a 120 L volume was used to evaluate the holder atmosphere control. Nitrogen was used as the purge gas which was delivered to the container with variable flow rates. Eq.2 was pre-calibrated with a purge gas flow rate of 100 L/min to obtain the factor  $\alpha$  and  $\beta$ . Varying the purging rate yielded results as shown in Fig.6. It was found that the oxygen concentration in the 120 L volume container can be lowered to less than 1% when the nitrogen flow rate was 110 L/min; whereas the oxygen concentration rate rose to 3% with a purge rate

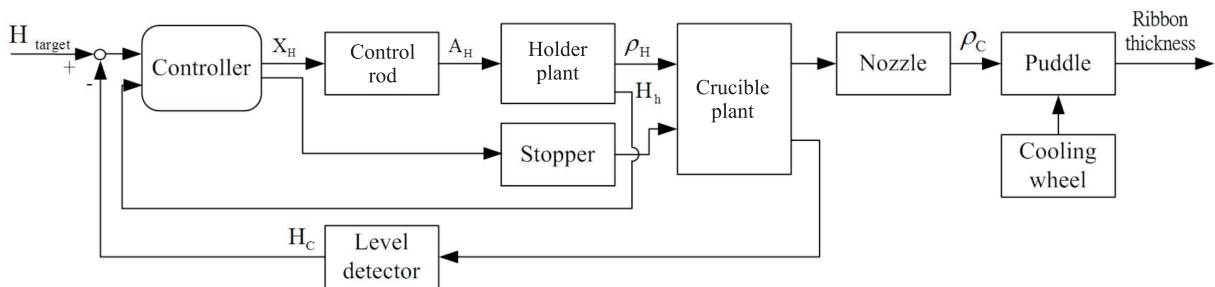


Fig.3. Block diagram of the level control system.

Control logic table		CL(ms)	OP(ms)	dC(mm)	dO(mm)	V(mm/ms)
Level & different		Close time	Open time	Close position	Open position	Open position
A	High & large	CLA	OPA	dCA	dOA	VA
B	High & medium	CLB	OPB	dCB	dOB	VB
C	High & small	CLB0	OPB0	dCB0	dOB0	VB0
D	Low & small	CLC0	OPC0	dCC0	dOC0	VC0
E	Low & small	CLC	OPC	dCC	dOC	VC
F	Low & large	CLD	OPD	dCD	dOD	VD

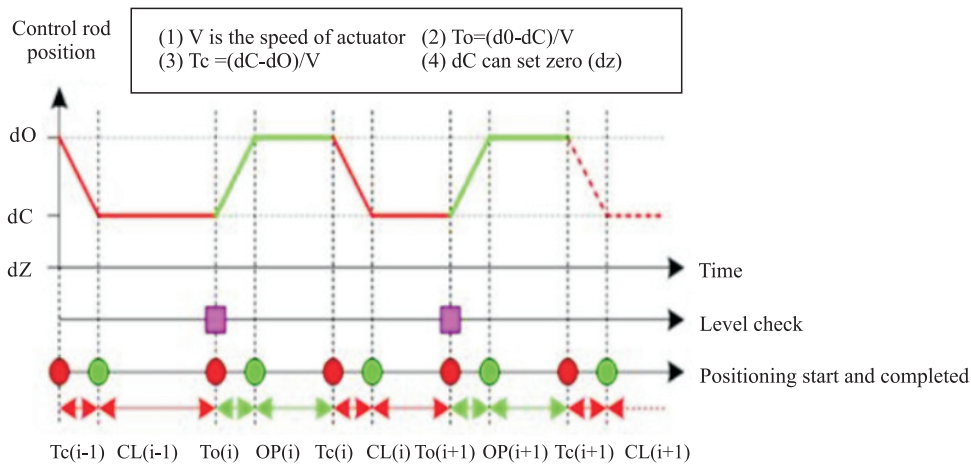


Fig.4. Control rod operating logic.

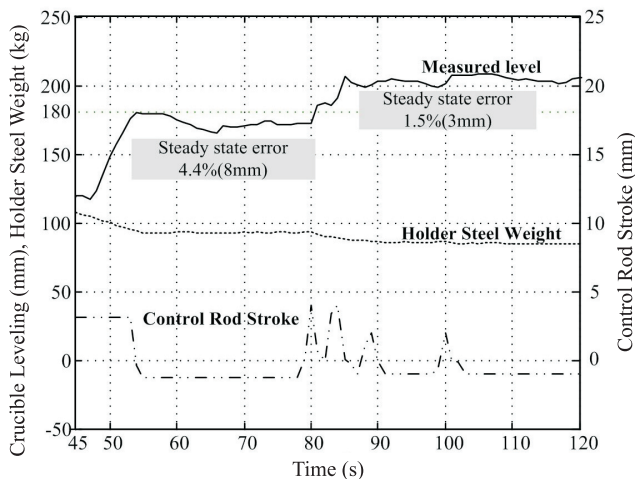


Fig.5. Level control experimental validation result.

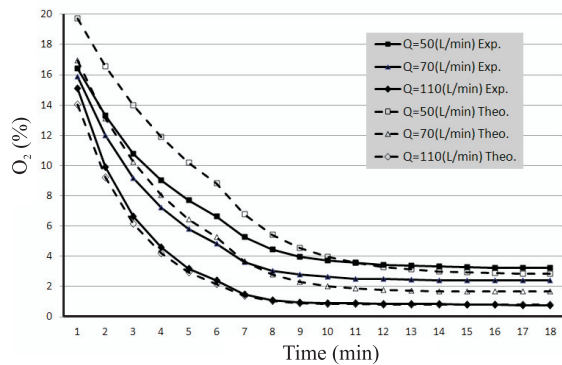
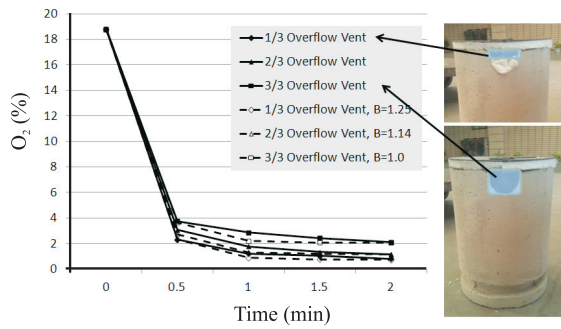


Fig.6. Theoretical and experimental results of oxygen concentration in a holder with different nitrogen volumetric flow rates.

of 50 L/min. It was also noticed the larger the flow rate of nitrogen, the more consistency between the theoretical and experiment results.

For the atmosphere control of the crucible, the off-line result showed when the nitrogen flow rate was 60 L/min, the oxygen concentration in the crucible (12 L volume) could be reduced to less than 1%. This

research also considered the realistic sealing condition of the crucible as the overflow vent represented a sealing variable. With different openings of the vent, the model yielded different degrees of accuracy. The discrepancy between the prediction and experimental results tended to increase as the vent opening increased (Fig.7).



**Fig.7.** Theoretical (dash line) and experimental results of oxygen concentration in crucible with different openings of the vent when the nitrogen flow rate is 60 L/min.

During the on-line test of the purging system, the temperature effect should also be taken into account. As the gas temperature rose from room temperature (298 K) to the holding temperature (1573 K), its volume expanded at least five times according to thermodynamics. This equivalently reduced the necessary purge gas rate by 5 times. Experimental results showed that only 20 L/min was required to lower the oxygen concentration rate to 0%, which had a fairly good agreement with the prediction.

One practical issue worth noting was the insulation material used, refractory wool, worked as a very poor sealing device at these high temperatures. Initially the sealing cap of the crucible was made from a combination of various high density wools. This resulted in at best 6% oxygen concentration due to rising porosity of the material at these high temperatures and pressures. Improvement showed that the oxygen concentration could be controlled to below 1% with a much lower purge gas rate by replacing the cap to a steel-refractory composite which met the requirements of the atmosphere control.

### 3.3 Cooling rate estimation

The cooling rate in the process is a critical factor as it ensures the quality of the amorphous formation. However, with the rapid changes in temperature, it was difficult to assess by direct measurement given the constraints of sensor response and spatial limitations around the puddle. A quick evaluation tool using an one-dimensional transient heat transfer model was developed to evaluate the cooling rate in the current system when casting the Fe-Si-B amorphous ribbon (Eq.3) The geometric domain of the problem is shown in Fig.8, where x-direction is the ribbon thickness,  $T_i$  the molten metal temperature,  $T_\infty$  surface temperature of the wheel,  $k$  thermal conductivity of the ribbon,  $\alpha$  the thermal diffusion coefficient of the ribbon and  $h$  the heat transfer coefficient of the wheel-ribbon boundary. Table 1 lists the model parameters and their values. The boundary condition of this case was assumed to be convective heat transfer shown in Eq.4. The solution of ribbon temperature varying with time can be expressed by Eq.5.

$$\frac{\partial^2 T}{\partial X^2} = \frac{1}{\alpha} \frac{\partial T}{\partial t} \dots\dots\dots (3)$$

$$-kA \left[ \frac{\partial T}{\partial x} \right]_{x=0} = hA [T_\infty - T(0,t)] \text{ for } t > 0 \dots\dots (4)$$

$$\frac{T(x,t) - T_i}{T_\infty - T_i} = \text{erfc} \left( \frac{x}{2\sqrt{\alpha t}} \right) - \left[ \exp \left( \frac{hx}{k} + \frac{h^2 \alpha t}{k^2} \right) \right] \left[ \text{erfc} \left( \frac{x}{2\sqrt{\alpha t}} + \frac{h\sqrt{\alpha t}}{k} \right) \right] \dots\dots\dots (5)$$

**Table 1** Parameters using in the cooling rate estimation of Fe-Si-B amorphous ribbon on a Cu-Be substrate

Parameters	Symbol	Value
Surface temperature of wheel	$T_\infty$ (°C)	30
Molten metal temperature	$T_i$ (°C)	1200
Thermal conduction coefficient of ribbon	$k$ (W/m*K)	30
Thermal diffusion coefficient of ribbon	$\alpha$ (m <sup>2</sup> /s)	$2.12 \cdot 10^{-5}$
Heat transfer coefficient of wheel (estimated from exp. data)	$h$ (W/m <sup>2</sup> *K)	105~106

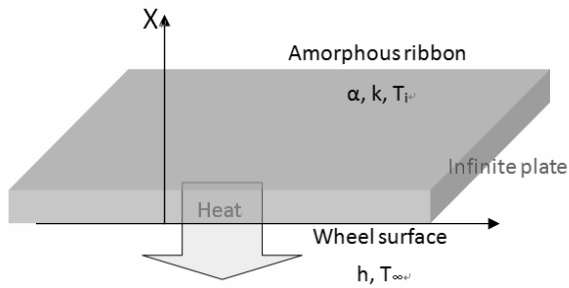


**Fig.8.** A simple illustration of the transient one-dimensional heat transfer model. The x-direction is ribbon thickness,  $T_i$  the molten metal temperature,  $T_\infty$  surface temperature of wheel,  $k$  the thermal conductivity of the ribbon,  $\alpha$  the thermal diffusion coefficient of the ribbon and  $h$  the heat transfer coefficient of wheel-ribbon boundary.

The surface temperature of the ribbon was measured by an IR sensor (Williamson PRO220-36) as it exited the puddle area. The ribbon temperature at the circumferential position of  $100^\circ$  around the wheel was approximate  $200^\circ\text{C}$  in our system. According to the measured ribbon temperature and the proposed heat transfer model, the heat transfer coefficient of the cooling wheel was estimated to be  $2.5 \times 10^5 \text{ W/m}^2\text{K}$ . The ribbon temperatures at different circumferential locations of the cooling wheel were estimated and plotted in Fig.9. It can be derived that the maximum cooling rate of the ribbon was  $1.77 \times 10^6 \text{ }^\circ\text{C/s}$  at  $1^\circ$ , which was corresponding to the puddle area, and the average cooling rate at  $0^\circ$  to  $5^\circ$ , where temperatures were above the glass transformation temperature, of the ribbon was  $6.9 \times 10^5 \text{ }^\circ\text{C/s}$  given that the ribbon thickness was  $25 \text{ }\mu\text{m}$ . Both of them were amid the range of the required theoretical cooling rate for amorphous materials.

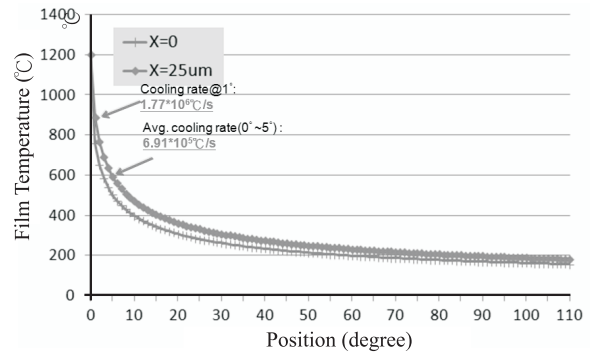


**Fig.9.** The ribbon temperatures at different positions of the cooling wheel at the bottom ( $x=0$ ) and top ( $x=25$ ) surface.

The ribbon temperature at the given location (i.e.  $100^\circ$  in the wheel rotational direction from the puddle in our system) was further analyzed with respect to the effect of the wheel cooling capacity and the ribbon forming thickness. With an increase in the capacity of the heat removal rate by 50%, the ribbon temperature could be reduced by approximately 25% from  $230$  to  $170^\circ\text{C}$ , (Figure 10, left). On the other hand, for the same cooling capacity of the wheel ( $2.5 \times 10^5 \text{ W/m}^2\text{K}$ ), the ribbon temperature rose as its thickness increased in a near linear fashion (Figure 10, right). Both characteristics were ideal indicators for process control in monitoring wheel surface conditions and ribbon thickness.

### 3.4 Tension control

Amorphous ribbon casting process has a relatively high throughput at the rate of 1200 to 1500 m/min. For the continuity of the process and prevention of scratching the surface quality of the ribbon, a winding process is necessary. However, the ribbon has low inertia and a thin gauge, it is extremely difficult for an in-line winding

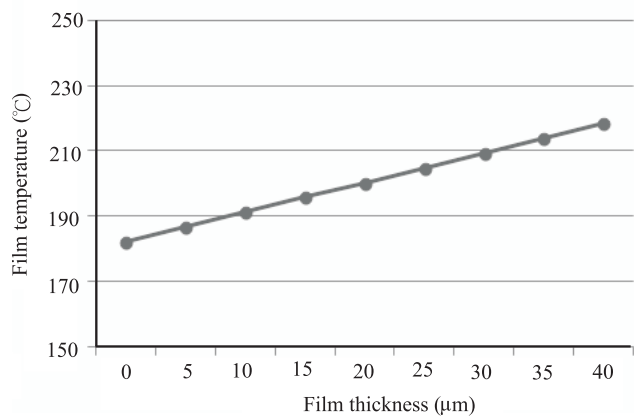
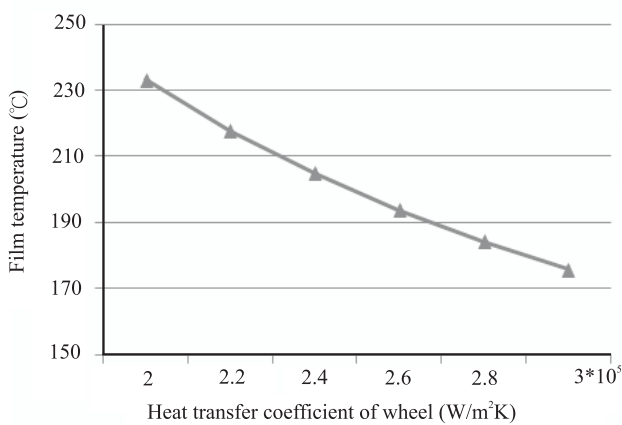


**Fig.10.** The calculation results of ribbon temperatures vary with heat transfer coefficient of wheel and film thickness at position of  $100^\circ$  in the wheel rotational direction from the puddle.

process. It is known that it is the key process in the commercial scale production of ribbon and very limited information regarding its implementation is available in any literature.

The winding process operation requires a constant speed and tension. Figure 11 shows a block diagram of the developed winding tension control system. A servo motor was used as the main drive as it provided enough bandwidth and precision for control. At the initial stage of the winding process, it was controlled by the speed mode in which target rotational speeds were given as inputs. For establishing a tension between the winder and casting wheel, a 1 to 2% linear speed mismatch between the two devices were introduced. As the process continued, many complications to the system were encountered, particularly the winding spool eccentricity due to the coils' loose form at a low tension, which in

turn caused tension variations that strongly impacted on the stability of the process. Furthermore, high stiffness of the ribbon and the lack of inter-stand rollers to act as tension isolators contributed to a high rate of ribbon breakages under the speed control mode. Ideally, there should be a tensiometer feedback to stabilize the process. In practice, an additional tensiometer and its supporting rollers in the path line would cause impossible threading and path control problems. Under such circumstances, it was proposed that after the threading process, the motor control should switch to a torque mode in which a target torque command is given. The target torque was derived by the required tension and the winding roll diameter (Fig.11). It was further constrained by a speed limit in case the ribbon broke.

Figure 12 shows the experimental result of the proposed winding control scheme. The diameter of the

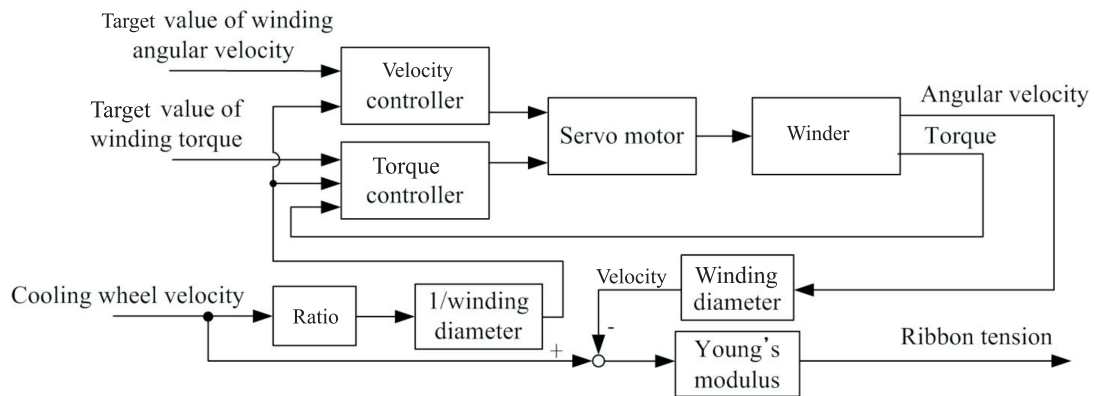


Fig.11. Block diagram of tension controller.

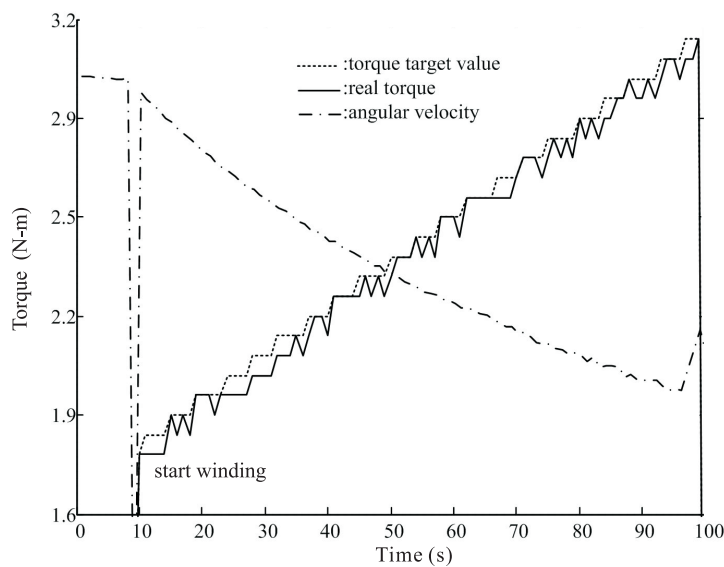


Fig.12. Tension control experimental results (casting # 1123).

winder increased as the ribbon was grabbed by the winder and the angular velocity of the winder was decreased accordingly to maintain a constant linear speed and ribbon tension. The measured torque was observed following the target value closely, which was estimated by the model. The process successfully lasted for a greater period of time which demonstrated the robustness and effectiveness of the control scheme.

**3.5 Evaluation of refractory**

There were 18 kinds of refractories developed in our amorphous pilot line, including the lining of the holder, control rod, submerged nozzle, upper nozzle, upper nozzle seat, crucible, stopper, float, casting nozzle, nozzle support, etc. The amorphous manufacturing process is different from that of the general steelmaking process, and so is the refractory requirements. For example, holder linings would not only resist the corrosion of silicon and boron-rich molten metal, but also need to insulate the chamber. Crucibles and nozzles are required to withstand harsh thermal shocks with a temperature gradient of more than 600°C, which is 300°C higher than that in typical steelmaking. Meanwhile they also need to resist erosion due to the high-velocity moving molten metal. Such diverse operating spectra and extreme conditions presented a great challenge in developing the refractories in the amorphous casting process. There are many aspects in the design process and only a few fundamental methodologies are reported below.

**3.5.1 Analytical design of the lining thickness**

The holding furnace requires high insulation which contains several insulating layers. The design of the lining thickness was based on a steady-state heat transfer model given by Eq.6,

$$Q = \frac{\lambda_1}{\ell_1}(t_1 - t_2) = \frac{\lambda_2}{\ell_2}(t_2 - t_3) = \dots = \frac{\lambda_n}{\ell_n}(t_n - t_{n+1})$$

$$= \frac{t_1 - t_{n+1}}{\frac{\ell_1}{\lambda_1} + \frac{\ell_2}{\lambda_2} + \dots + \frac{\ell_n}{\lambda_n}} \dots\dots\dots (6)$$

Where  $Q$  is the heat flux through the wall (kcal/m<sup>2</sup>. h),  $\lambda_n$  the thermal conductivity of the n<sup>th</sup> layer,  $\ell_n$  the thickness of layer  $n$ ,  $t_n$  the interface temperature between the nth and n+1 layers. Associated material parameters of holder lining are shown in Table 2. Experimental verification found that after heating the chamber for 8 hours and holding it at 1400°C, temperatures at the insulation interfaces correspond with predictions, as shown in Table 2 and Fig.13. This allows the holder to operate at a desired temperature with the cold face temperature below a safety limit of 200°C.

**3.5.2 Corrosion test**

To ensure the lining was inactive to the molten metal ingredients, corrosion tests were developed to quantitatively evaluate the materials' resistance to the Fe-Si-B alloy. Materials in Table 3 were cast into cylindrical crucibles with a 30 mm diameter and 50mm high, cured at room temperature for 24 h, and then dried at 110°C for another 24 h. Fe-Si-B pellets were placed in the crucible and then heated at a rate of 10°C /min and held at 1300°C for 3 h. The crucible with the molten alloy was then cooled naturally in the furnace and then dissected at the center for further observation. Penetration depths in Table 4 showed that Al<sub>2</sub>O<sub>3</sub>-MgO castable had a better corrosion resistance than the MgO coating and MgO gunning, as shown in Fig.14. It was suitable as a working lining for the holder as it maintained contact with the melt for a longer period of time.

**3.5.3 Thermal shock damage test**

The crucible sample materials in Table 3 were cast and prepared as specimens with dimensions of 40 mm ×40 mm×160 mm (JIS standard R-2575), cured at room temperature for 24 h, dried at 110°C for another 24 h, fired at 1400°C for 3 h and then cooled naturally. The specimens then underwent repeated cycles of heating and quenching. Each cycle started with heating the specimen at 1000°C for 30 min and followed by forced air cooling. Twelve identical cycles were performed on each sample. Upon finishing the thermal shock process, cracks on each sample were visually inspected. In

**Table 2** Material parameters of holder refractory lining

Layer	Thickness (mm)	Materials	Thermal conductivity (Kcal/mh°C)	Estimated interface temperature (°C )	Measured temperature (°C )
1 <sup>st</sup>	50	Al <sub>2</sub> O <sub>3</sub> - MgO castable	1.6	1128	1105
2 <sup>nd</sup>	85	Insulating castable	0.42	485	470
3 <sup>rd</sup>	65	Insulating brick	0.215	123	-
4 <sup>th</sup>	20	Iron shell	41	122	-

**Table 3** Tested materials for the holder, crucible and casting nozzle

Part	Material
Holder	MgO coating, MgO gunning and Al <sub>2</sub> O <sub>3</sub> - MgO castable.
Crucible	Al <sub>2</sub> O <sub>3</sub> - MgO -C, Al <sub>2</sub> O <sub>3</sub> -SiC -C and Al <sub>2</sub> O <sub>3</sub> -C castable.
Casting nozzle	Al <sub>2</sub> O <sub>3</sub> - MgO, Al <sub>2</sub> O <sub>3</sub> - MgO -C, Fused silica complex, non-oxide.

**Table 4** Corrosion test result

Material	Corrosion rate (mm/h)	Penetration depth (mm)
MgO coating	~2.5	10
MgO gunning	~3.0	15
Al <sub>2</sub> O <sub>3</sub> - MgO castable	~0.01	0.8~6.8

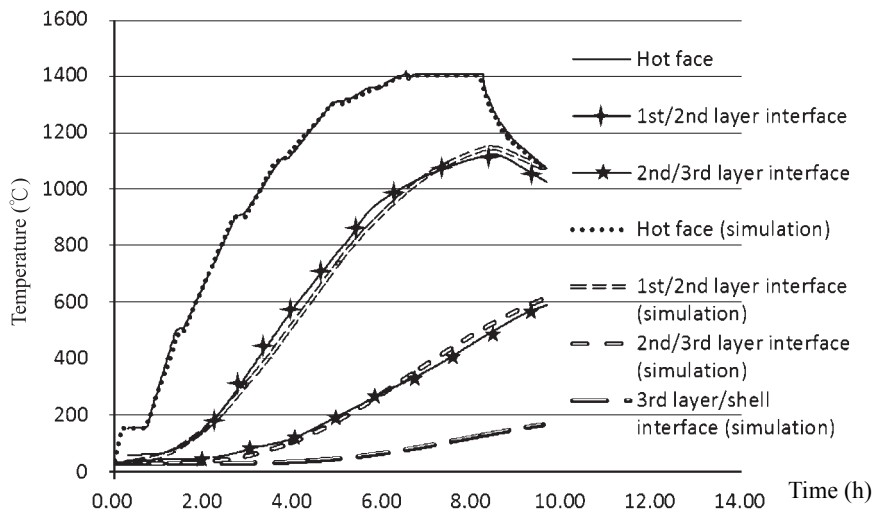


**Fig.13.** Experimental temperature profiles at each lining interface of the holder.

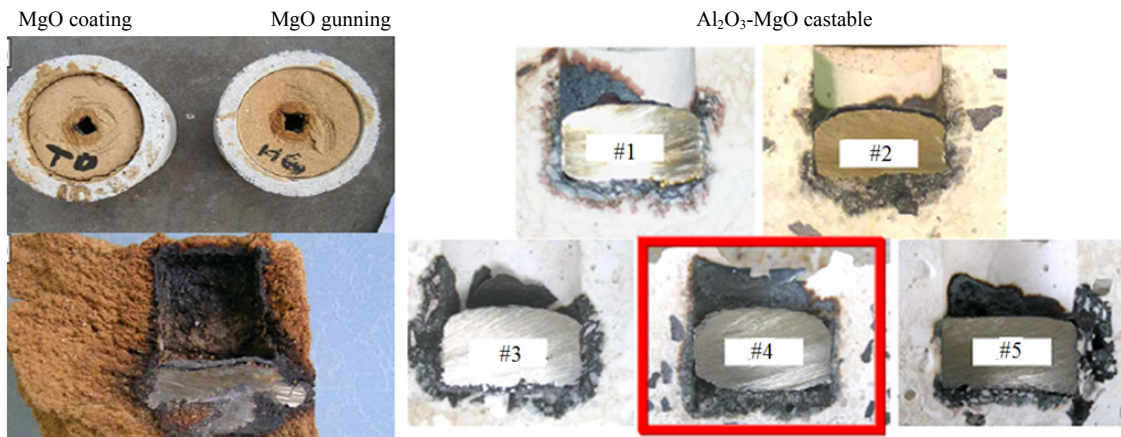


**Fig.14.** Corrosion test result and residual samples of holder evaluation material: MgO coating, MgO gunning and Al<sub>2</sub>O<sub>3</sub>- MgO castable.

addition, rupture modulus tests were performed to identify samples' residual strength and compared with those before the thermal cycles. The results in Table 5 showed that the alumina-carbon castable had better residual strength than Alumina-magnesia-carbon, alumina-silica-carbon castable, as shown in Fig.15. It was the ideal material for the use in the crucible.

### 3.5.4 Thermal expansion evaluation

Equipment in the amorphous casting process consists of a variety of refractory parts mating with each other. The thermal expansion of each component was expected to be minimal so not to generate too much internal thermal stress at their interfaces. The lining life duration will also benefit from low thermal expansion properties as the part undergoes heating cycles and experiences repeated contraction and expansion. The candidate material was cast into a specimen with dimensions of 5 mm×5 mm×25 mm, which was later placed in a thermal expansion measurement meter (Orton DIL-2016-STD dilatometer) with a heating rate of 10°C/min from room temperature to 1400°C.

The results showed that the expansion coefficient of alumina-magnesia, and alumina-carbon materials were about 5 to 8 ppm/°C. The expansion coefficient of fused silica complex was approximately 0.5 ppm/°C only and began to shrink at about 1070°C, as shown in Fig.16. Care should be exercised at this turning point. This information served as a critical design guideline in

component dimensions and tolerances. Note that the results may not be identical to other publications due to some proprietary casting agents and additives.

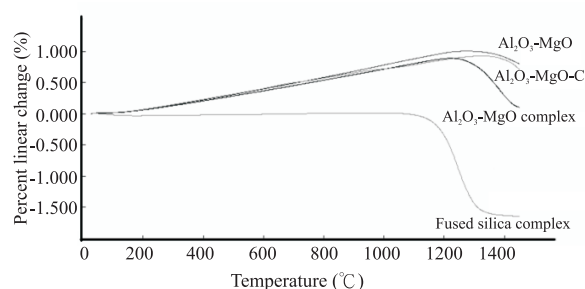


Fig.16. Thermal expansion test result for casting nozzle.

### 3.5.5 Simulation study

Transient thermal finite element models using ANSYS were established to provide more predictions regarding the material's performance in real usage. The primary interest was the thermal stresses on the crucible and casting nozzle during a real heat cycle so that the material strength can be appropriately designed. Six hypothetical materials for the nozzle and one for the crucible were analyzed. Their parameters including density and thermal conductivity, thermal expansion coefficient, young's modulus, etc. are listed in Table 6.

Table 5 Thermal shock damage test result

Materials	Alumina-magnesia -carbon castable	Alumina-carbon castable	Alumina -andalusite -carbon castable
1400°C, 3 h MOR (kg/cm <sup>2</sup> )	499	561	410
After thermal shock, MOR (kg/cm <sup>2</sup> )	73 (1 pc broken)	69	34 (1 pc broken)
Residual strength ratio (%)	14.5	12.0	8.2



Fig.15. The thermal shock damage test for crucible refractories (left: heated, right: cold).

**Table 6** Refractory thermal and mechanical properties used in the simulation

Material	Density (kg/m <sup>3</sup> )	Thermal conductivity (W/m°C)	Thermal expansion coefficient (10 <sup>-6</sup> /°C)	Young's modulus (GPa)	Poisson ratio	Heat capacity (J/kg°C)
A	3900	28	8	370	0.26	880
B	3300	27	2.3	310	0.24	700
C	2203	1.3	0.55	71.7	0.17	754
D	2200	16	3.1	180	0.2	700
E	3200	17	3.2	300	0.28	700
F	3050	40	3.3	300	0.28	700
Crucible	3000	1.744	5.0	20	0.2	1080

According to a given heating pattern, the model predicted the maximum thermal stress occurring at the middle barrel of the crucible, as shown in Fig.17. The experiment result (Fig.18) shows a similar crack suggesting the model accuracy. The model was later used in fine tuning the crucible design and modifying the heating pattern.

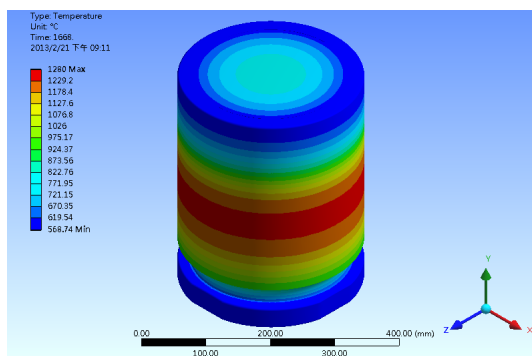
The thermal stress analysis for a casting nozzle showed that the stress concentrated at the bottom surface, where the largest deformation took place (Fig.19). Detailed examination revealed that the thermal gradient at the nozzle part exceeded initial design limits. A change in material by selecting a higher conductivity and lower thermal expansion refractory (e.x. Material B, D, E, F) successfully controlled the stress and deformation within the functional limits, which was further verified on the hot test.

#### 4. RIBBON QUALITY ISSUES

##### 4.1 Dimension control

Dimension control of the ribbon is an important quality topic for applying the product in the field such

as transformer cores. Since the width of the ribbon is determined by the nozzle slit and remains invariant during the process, the thickness is the only controlled geometric parameter. Many researchers have shown the relationship between process parameters and the ribbon thickness<sup>(5,6)</sup>. The molten metal flow in the puddle region was assumed to be inviscid and can be modeled analytically by combining mass and Bernoulli balances. This would yield the ribbon thickness as a function of the gap, casting pressure and wheel surface speed as shown in Eq.7<sup>(5)</sup>. A free fall casting process was developed to characterize the main variables in this equation. During the experiment the casting pressure, which was determined by the molten metal levels, was continuously decreased to generate a wide range of inputs for Eq.7. The true level of molten metal ( $\Delta P$ ) was measured by a float rod in conjunction with a load cell in the crucible. The gap (G) data was continuously monitored with a CCD image system. Other important parameters were detailed in Table 7. Numerical curve fitting using the experimental data and parameters in Table 7 yielded the unknown characteristic parameters a, and b to be 2 and  $5.5e^5$ , respectively.

**Fig.17.** Thermal stress analysis result of crucible.**Fig.18.** Crucible crack during the test.

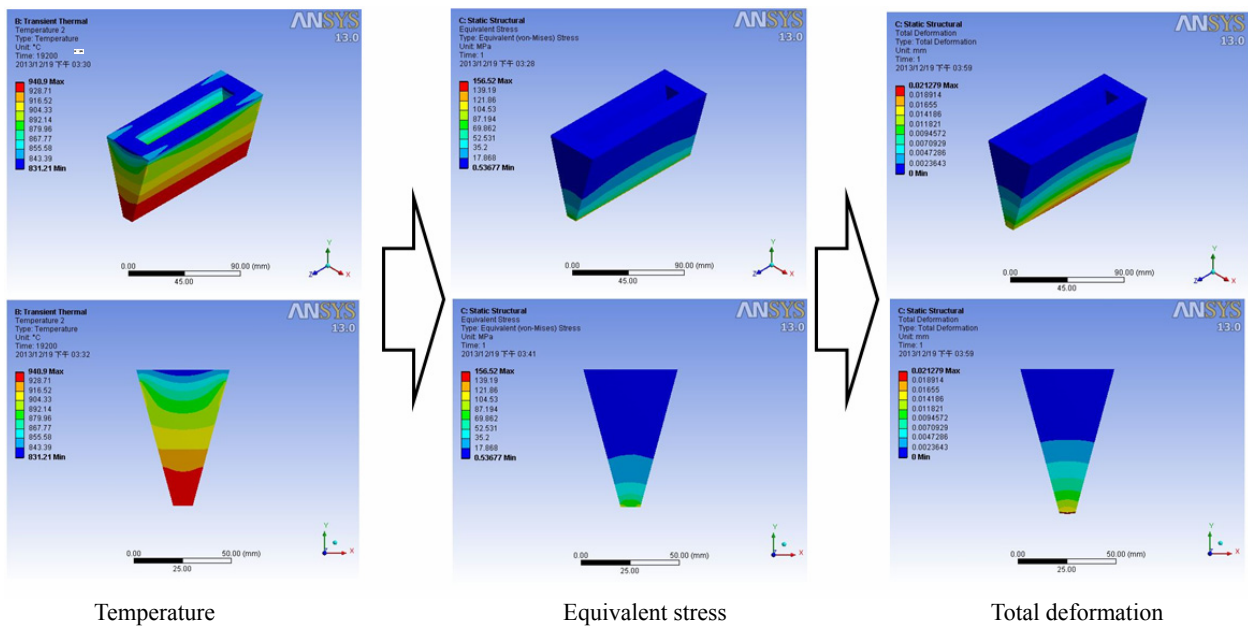


Fig.19. Thermal stress analysis result of casting nozzle.

Table 7 Parameters used in the ribbon thickness estimation model

Parameters	Symbol	Value
Ribbon thickness	T (μm)	15~35
Gap	G (mm)	0.2~0.4
Float level	ΔP (mm)	100~270
Density of ribbon	ρ (kg/m <sup>3</sup> )	7400
Surface speed	U (m/s)	20
Coefficient (Estimated)	a, b	2 & 550000

$$\left(\frac{T}{G}\right)^a = b\left(\frac{\Delta P}{\rho U^2}\right) \dots\dots\dots (7)$$

Three offline measurements of ribbon thickness were also labeled in Fig.20. They were in good agreement with predictions which implied the model accuracy. The model thus could be utilized in the on-line operation for precisely control of amorphous ribbon thickness.

**4.2 Surface quality**

The magnetic properties of amorphous ribbon are influenced by defects on the ribbon surface. These defects can be due to inclusions, strains or surface irregularities. In the case of planar flow casting, air bubbles are trapped on the underside of the molten steel upon contact with the quenching wheel surface. In consequence, a pattern of air pockets on the wheel side of the ribbon results. It was noted that the air side of the ribbon would also exhibit the similar features with decayed dimensions. The air entrainment would form a

high thermal resistance layer impeding the heat dissipation of the molten metal which has a profound effect on the strain distribution around the pocket. The magnetic properties are also strongly affected by these types of features.

Many control schemes have been proposed in published writings to reduce air pockets of the amorphous ribbon, such as atmosphere control, varying roughness of wheel surface, increasing wettability of molten steel on the wheel, increasing casting pressure, reducing gap between nozzle and wheel, increasing wheel speed and lowering superheat<sup>(7,8)</sup>. In this research, casting pressure and the roughness of the wheel surface have been evaluated to minimize the size and the population of air pockets.

Figure 21 shows the Optical Microscope (OM) image (50X) of an amorphous ribbon at different casting time. At the start of casting (0 sec), the size of air pocket on the ribbon was larger than the others due to initial instability of the puddle formation. The air pocket size, which was calculated by square root of the air pocket area, increased as the cast carried on during

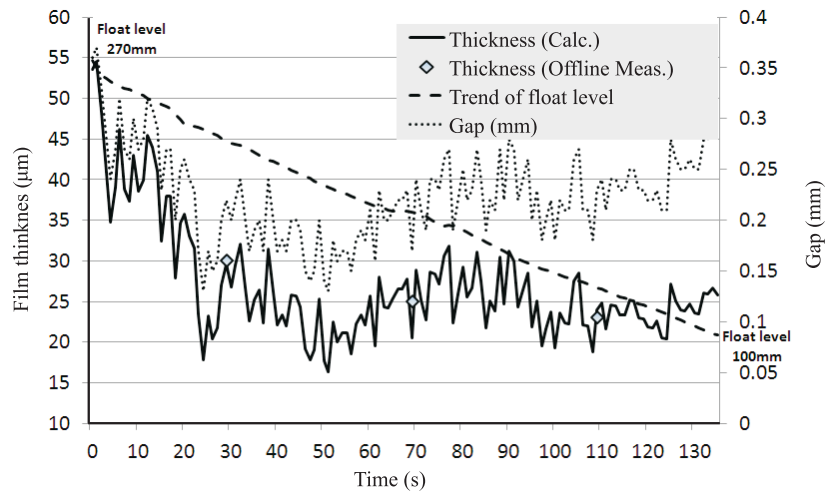


Fig.20. Calculated ribbon thickness (solid), gap and float level (cast #1191).

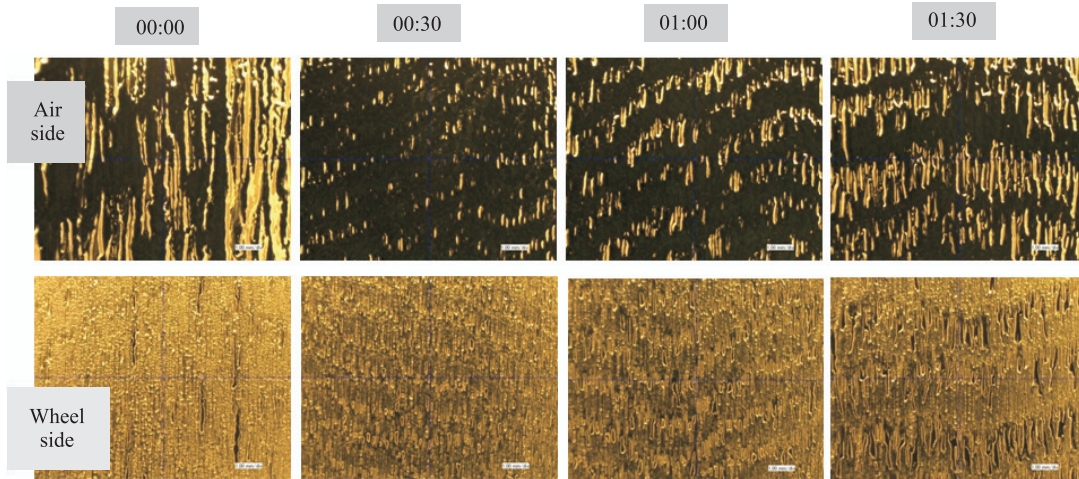


Fig.21. Optical Microscope (OM) image (50X) of a ribbon at different casting times.

which the pressure was continuously decreasing (Fig.22). This suggested that the air pocket dimension was inversely proportional to the casting pressure. It could be attributed to that the entrained gas volumetric growth due to heat was limited by higher liquid pressures<sup>(7)</sup>.

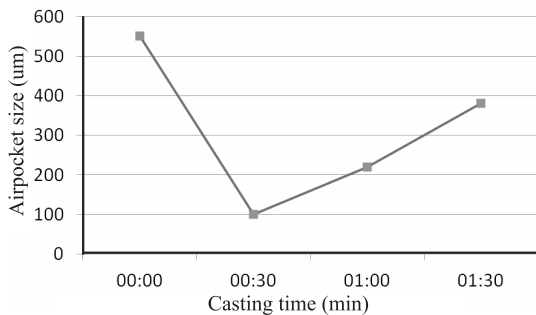


Fig.22. Air pocket size of amorphous ribbons at different casting times.

Cooling substrate roughness was able to alter the formation of the air boundary layer upon the wheel surface and affect the dimension of the air pockets. During the tests, the wheel surface was prepared with different orders of roughness ranging from 0.1 to 1 µm. Figure 23 shows the Optical Microscope (OM) images (50X) of the amorphous ribbons in varying wheel roughness tests. It was observed that there existed an optimum roughness range, between Ra 0.3 to 0.6 µm, for minimum pocket sizes (Fig.24). This can be attributed to a critical wetting pattern of the liquid metal on the casting wheel surface and that resulting to less air entrapped between the liquid metal and the wheel<sup>(8)</sup>.

### 4.3 Magnetic properties

The magnetic properties of amorphous ribbons are influenced by magnetic anisotropies of ribbon structure and surface. Owing to the lack of atomic long-range order, stress and shape anisotropies determine the

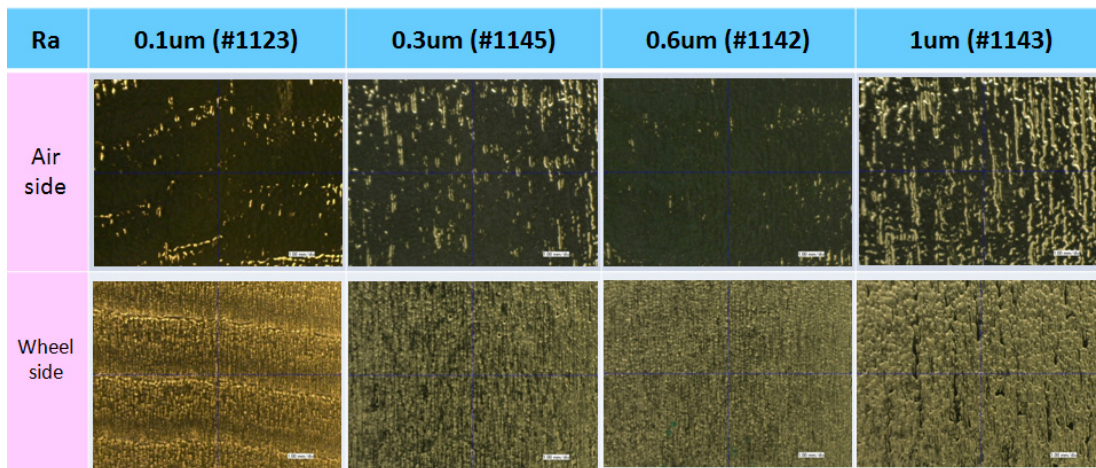


Fig.23. Air pocket variation with respect to wheel roughness.

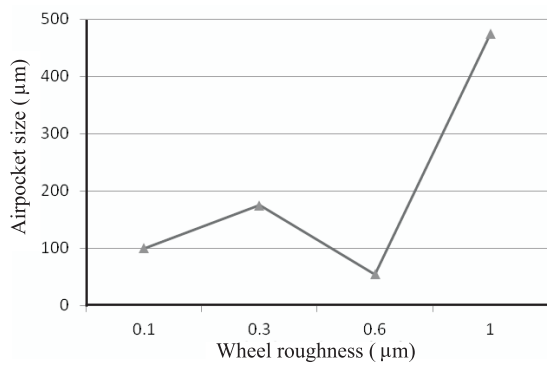


Fig.24. Air pocket size of amorphous ribbons using different wheel roughness (Ra).

macroscopic magnetic properties. The shape of anisotropies can be due to inclusion, air pocket, or surface irregularities, all of which impede magnetic domain wall motion. The stress anisotropy arises from the cou-

pling between mechanical stresses and magnetization via magnetostriction, and such stresses are induced during the fabrication procedure.

Annealing can alter the magnetic easy axis of induced magnetic anisotropy by applying a magnetic field during the process. The ribbon was annealed in a custom-made annealing furnace with a field of 800 A-m. Several annealing temperatures were applied to evaluate their effects on the magnetic properties. A post annealing process further characterized the ribbon's hysteresis loop in the casting direction by a vibrating sample magnetometer device (VSM, MicroSense EZ series) up to 1.5 T, which measured the magnetic moments of a sinusoidally vibrating sample in a uniform magnetic field. Figure 25 shows the coercivity ( $H_c$ ) and saturation magnetization ( $M_s$ ) measured in the VSM for as-cast and annealed ribbons. It was found that an increase in temperature leads to a reduction in  $H_c$  but no obvious changes in  $M_s$ . This is attributed to the

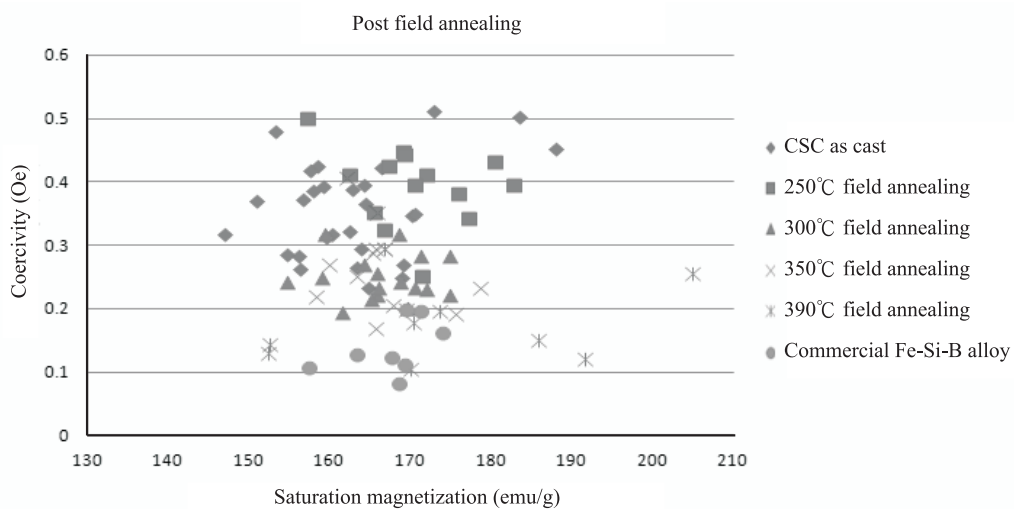


Fig.25. Magnetic properties of amorphous ribbons with different annealing temperatures.

rearrangement of magnetic domain with an external magnetic field. The curie temperatures of CSC ribbon were further characterized and found between 395 to 410 °C. Results suggest that the best annealing temperature for the lowest coercivity and saturation magnetization of the ribbon is close to but not over the curie temperature of amorphous ribbon.

#### 4.4 Annealing embrittlement

Annealing treatment of amorphous alloy for improving magnetic properties is essential. However the amorphous alloy becomes brittle when heated at temperatures several hundred degrees below their glass transition temperature. This could leave the ribbon unprocessable to downstream processes. Studies found a boundary line for embrittlement in the amorphous alloy for various binary combinations of transition-metal elements<sup>(9,10)</sup>. The stability of amorphous metallic alloys being of an iron base has been reported previously<sup>(11,12)</sup>. It was shown that the embrittlement temperature was around 225 °C for iron-based amorphous below 82 at % of Fe as the activation energy and mixed entropy significantly rose above that temperature.

The ribbon ductility after annealing treatment was measured by means of a bend test in collaboration with J. R. Yang<sup>(13)</sup>. The temperature that the amorphous ribbon appeared brittle was from 310 to 360 °C. In the previous section, it was suggested that higher temperatures, particularly close to the curie temperature, was advantageous to lower the coercivity. However, the upper part of this temperature range could inevitably lead to embrittlement. Considering both in ductility and magnetism, our study suggested that the annealing temperature should be between 350 to 360 °C.

#### 4. CONCLUSIONS

A 200 kg pilot plant for iron-based amorphous manufacturing was established at CSC. Important engineering achievements are summarized below

- (1) The molten melt flow rate was regulated by the control rod. A fuzzy-like lookup table control strategy was adapted and showed a steady state error in the order of 1.5% range.
- (2) A well-mixed model was developed for assessing the required purge gas flow rate. The cold and hot tests revealed the model accuracy with extending adjustment on gas thermal expansion. The oxygen concentration rate could be lowered to 1% based on the calculated purge rate.
- (3) A one dimensional heat transfer model estimated the maximum cooling rate of the current system was  $1.77 \times 10^6$  °C/s.
- (4) The winding tension control was realized by mixed control modes, including the speed mode at the threading stage and torque at the winding stage. Experiment results showed that the system could operate for a longer period of time at the rate of 1200 m/min.
- (5) Air pockets on the ribbon surface could be alleviated by increasing casting pressure and optimizing the wheel roughness.
- (6) The optimum ribbon annealing temperature was in the range of 350 to 360 °C considering improving ribbon's magnetic properties and preventing embrittlement of the ribbon.

#### REFERENCES

1. N. DeCristofaro: MRS Bulletin, 1998, vol. 23, no. 5, pp. 50-56.
2. H. H. Liebermann: Journal of Crystal Growth, 1984, vol. 70, no. 1, pp. 497-506.
3. R. W. Jech: JOM, 1984, vol. 36, no. 4, pp. 41-45.
4. Y. Sahai, Y. and E. Toshihiko: Tundish Technology for Clean Steel Production, World Scientific Publishing Company, 2007.
5. E. A. Theisen: Transient Behavior of the Planar-Flow Melt Spinning Process with Capillary Dynamics, PhD Dissertation, Cornell University, 2007.
6. D. Li, J. Zhuang, T. Liu, Z. Lu and S. Zhou: J. Mater. Processing Technology, 2011, vol. 211, no. 11, pp. 1764-1767.
7. H. Fiedler, H. Mühlbach and G. Stephani: J. Mater. Sci., 1984, vol. 19, no. 10, pp. 3229-3235.
8. S. C. Huang and H. C. Fiedler: Metall. Trans. A, 1981, vol. 12A, pp. 1107-1112.
9. F. E. Luborsky and L. Walter: J. Appl. Phys. 1976, vol. 47, pp. 3648-3650.
10. T. Masumoto and R. Maddin: Mater. Sci. Eng., 1975, vol. 19, pp. 1-24.
11. S. Takayama: J. Mater. Sci., 1976, vol. 11, pp. 164-185.
12. M. Gyorgy, H. J. Leamy, R. C. Sherwood, H. S. Chen, AIP Conf. Proc., 1976, vol. 29, pp. 198-203.
13. J. R. Yang: RE99040 Report, China Steel, 2011. □